Biosensors and Bioelectronics 127 (2019) 135–141

Contents lists available at ScienceDirect

Biosensors and Bioelectronics

journal homepage: www.elsevier.com/locate/bios

An electrochemical biosensor based on novel butylamine capped CZTS nanoparticles immobilized by uricase for uric acid detection

Shefali Jain[a,b], Shilpi Verma[a,b], Surinder P. Singh[a,b], Shailesh Narain Sharma[a,b,*]

[a] Academy of Scientific and Innovative Research (AcSIR), CSIR- Human Resource Development Centre, (CSIR-HRDC) Campus, Ghaziabad, Uttar Pradesh 201 002, India
[b] CSIR-National Physical Laboratory (NPL), Dr. K.S. Krishnan Road, New Delhi 110012, India

ARTICLE INFO

Keywords:
Butylamine capping ligand
Tunable band gap CZTS
Colloidal route
Amperometric bio-sensor
Uric acid

ABSTRACT

Quaternary chalcopyrite, i.e., Cu_2ZnSnS_4 (CZTS) nanoparticles films have been proposed as a novel matrix system for enzyme-based electrochemical biosensors providing a non-toxic, low-cost alternative for the fabrication of bioelectrodes. The easy tuneability of the band gap of CZTS by varying the cation ratio and size of nanoparticles facilitate to impart desirable electrical properties in the material. Butylamine capped spherical CZTS nanoparticles of size 15–16 nm and band gap 2.65 eV have been synthesized by colloidal hot injection technique. The films of CZTS onto ITO substrates are deposited using dip coating technique, and uricase enzyme have been immobilized onto CZTS films using EDC-NHS binding chemistry. Electrochemical analyses of this bioelectrode revealed that the uricase/CZTS/ITO/glass electrode exhibits good linearity over a wide range of 0–700 μM uric acid concentration with a limit of detection (LOD) of 0.066 μM. The low value of 0.13×10^{-4} M of Michaelis–Menten constant (K_m) indicate the enhanced affinity of immobilized enzyme (uricase) towards uric acid. Thus, the present report confirms the promising application of the p-type CZTS thin film matrix for the realization of an electrochemical biosensor.

1. Introduction

In today's state of health, it is an imperative requirement to develop the more sophisticated, classy, reliable device to sense biological, biochemical and enzymatic analyses for application in the different area of medicine. Uric acid ($C_5H_4N_4O_3$) acts as an antioxidant, found in urine or blood serum excreted by kidneys as an end-product of metabolism process of the purine nucleotide and is responsible for many biological changes in the human body (Arora et al., 2011; Goyal et al., 2005). The increased amount of uric acid (UA) in body fluids from its normal range (i.e. 0.1–0.4 mM in blood and 1.5–4.4 mM in urine)(Nery, 2016) can lead to many diseases like gout, hyperuricemia, or Lesch-Nyhan syndrome, kidney disease and cardiovascular disease (Arora et al., 2011), thus making it important to monitor UA regularly. The most common method for UA detection is the enzyme-based electrochemical sensor which involves the oxidation of UA in the presence of uricase enzyme to give water-soluble allantoin and electro-oxidizable hydrogen peroxide.

Recent studies for the advancement in the field of biocompatible nanomaterials and biotechnology resulted in the improvement of the third-generation biosensor, based on the direct charge transfer phenomenon between the biological recognition element and the electrode. Various materials like polyaniline, polypyrrole nanoelectrodes, ZnO, CuO, graphene oxide, have been employed for the enzyme-based biosensors involving oxidation and reduction of hydrogen peroxide (Ali et al., 2012; Erden and K l ç, 2013; Roushani et al., 2014; Wang et al., 2014). However, these material systems are restrained due to slow electrode kinetics and high overpotential resulting into the decreased charge transfer and increased interferences from other electroactive species coexisting with the sample thus reducing the sensing capabilities of the devices based on these materials (Chen et al., 2012; Goux et al., 2006; Shinagawa et al., 2015). CZTS being a non-toxic, low cost with earth-abundant constituents is a direct band gap ($E_g \sim 1.4$–1.6 eV) semiconductor. It has high concentrations of acceptor Cu_{Zn} anti-sites and Cu vacancies which impart p-type conductivity to it, and high charge transfer capabilities (Chen et al., 2013; Zhou et al., 2012). Owing to extraordinary physicochemical properties such as good photostability, high carrier mobility, heat resistance, and long diffusion lengths, CZTS applications other than photovoltaics encompasses H_2 production, Li-ion batteries, thermoelectric, gas sensor and biomedicine (Gurav et al., 2014; Shinde, 2015; Wang et al., 2017; Yang et al., 2012). Despite versatile physicochemical properties and applications, the CZTS have not yet been explored in the field of biosensing. Ibraheam et al. have used Cd-doped quaternary alloy ($Cu_2Zn_{1-x}Cd_xSnS_4$) for the diagnosis of dengue fever using specific DNA sequence (Ibraheam et al.,

* Corresponding author.
E-mail address: shailesh@nplindia.org (S.N. Sharma).

https://doi.org/10.1016/j.bios.2018.12.008

Available online 13 December 2018

2016). CZTS quaternary inorganic-materials have also exhibited excellent antimicrobial activity against a range of bacterial pathogens (Kumar et al., 2015).

In spite of so many synthesis techniques like vacuum-based PVD techniques and other methods like co-evaporation, solvothermal etc. (Lee et al., 2015; Yoo and Kim, 2010; Zhou et al., 2011) we are using hot-injection technique owing to its simplicity, cost-effectiveness and non-involvement of a vacuum system for the synthesis of CZTS nanoparticles and introducing novel butylamine as a capping ligand for its application in the enzymatic electrochemical-biosensor, for sensitive detection of uric acid. Biocompatible and wide-bandgap CZTS nanoparticles have been synthesized using hot injection colloidal route method.

The butylamine capped CZTS nanoparticles were deposited onto ITO-coated glass substrate for the fabrication of electrode. The butylamine enables efficient covalent immobilization of enzyme molecules on CZTS surface thus eliminating the need for additional functionalization step. Uricase enzyme has been immobilized onto the butylamine functionalized CZTS surface through EDC-NHS chemistry. The fabricated biosensor exhibited enhanced response towards sensing of different samples having varied amount of uric acid. Moreover, the biocompatibility of CZTS nanoparticles helps enzymes to maintain their activities and hence contribute to enhanced shelf-life.

2. Experimental

2.1. Materials

Copper (II) chloride ($CuCl_2$), Zinc chloride ($ZnCl_2$), stannous chloride ($SnCl_4$), and elemental S were taken as precursors for CZTS synthesis. Butylamine ($C_4H_{11}N$) was taken as a solvent for different salts and acts as a capping ligand. Elemental S was dissolved in Tri-Octyl phosphine ($(C_8H_{17})_3P$ or TOP, 90%). For biosensor, Uricase enzyme (U3500 Uricase from bovine kidney ~15 units/g protein (biuret)), EDC (N-(3-dimethylaminopropyl)-N′- ethyl carbodiimide hydrochloride) of high quality and NHS (N-hydroxysuccinimide) were used, which acts as a binder. All the chemicals were of analytical grade and purchased from Sigma Aldrich.

2.2. Preparation of CZTS thin film

A homogeneous solution of CZTS nanoparticles was prepared by mixing 10 mg CZTS in 1 mL toluene. An area of $5 \times 5\ mm^2$ ITO was coated with CZTS nanoparticles at a dipping speed of 60 cm/mm, with assembling time and drying time being 1 min each. Each film was dipped 50 times to achieve required thickness of 50–70 nm.

2.3. Immobilization of Uricase on CZTS thin film

The stock solution of Uricase (1 μM) was freshly prepared in phosphate buffer (0.05 M, 0.9% NaCl) with pH value 7.0. An aqueous solution of EDC:NHS was prepared by mixing 0.5 M EDC and 0.1 M NHS in 1:1 (v/v) ratio. This solution was mixed with 1 μM uricase solution and incubated for 2.5 h for the activation of -COOH group. The bioelectrodes were fabricated (Fig. SI-2) by immobilizing 40 μL of the prepared uricase/(EDC:NHS) mixture on the thin films and incubating them for 4 h.

2.4. Synthesis and characterization

CZTS nanocrystals were synthesized using hot injection technique elaborated in previous literature with few modifications (Jain et al., 2018a, 2018b). The metal ion precursors were mixed in specific ratio (Zn/Sn = 4 and Cu/(Zn + Sn) = 0.5) in butylamine in an inert environment at ~300 °C. A change in color of reactants during reaction were observed from royal blue to peacock green and finally coffee brown color (Fig. SI-1) indicating the reduction of precursors.

The structural analysis of synthesized CZTS nanoparticles was carried out using Bruker-AXS D8 Advanced X-Ray diffractometer. and Transmission Electron Microscopy (TEM) measurements using JEOL electron microscope (JEM-200CX with an acceleration potential of 200 kV). Raman Spectra was measured via Renishaw Raman spectrometer in the range of 100–500 cm^{-1} with the excitation wavelength of 514 nm. The CZTS nanoparticles were imaged using Zeiss EVO MA-10 variable pressure SEM of resolution 3 nm with a probe current of 100 picoamps. FTIR spectra were recorded in the range of 400–4000 cm^{-1} using a Perkin Elmer instrument (Spectrum BX-500). X-ray photoelectron spectroscopy (XPS) measurements, were performed in an ultra-high vacuum chamber with a base pressure of $\sim 4 \times 10^{-10}$ Torr. Absorption curve is measured by using Cary 5000 dual beam UV–Vis–NIR spectrophotometer from 350 to 1100 wavelength range. Electrochemical measurements of bioelectrodes were carried out using compact PalmSens3 electrochemical interface equipped with three-electrode cell-configuration where silver/silver chloride (Ag/AgCl) electrode served as the reference electrode while the platinum wire mesh served as a counter electrode), in 3 mM Zobell as a redox indicator. Electrochemical impedance spectroscopy (EIS) measurements were recorded at an AC stimulus of 0.2 V in the frequency range of 0.1 Hz to 100 kHz using Metrohm Autolab.

3. Results and discussion

3.1. Structural analysis

XRD spectra of CZTS nanoparticles deposited in thin-film form have been obtained to depict the crystal structure and crystallite size (Fig. 1). The diffraction peaks appeared at a 2θ value of 28.61°, 47.60°, and 56.32° corresponds to the (112), (220), and (312) characteristic planes confirm the formation of kesterite phase CZTS (JCPDS 26-0575). The crystallite size of particles, calculated by Debye Scherer's formula (Chung et al., 2013) corresponding to major peak (112) was found to be approximate ~16 nm. However, XRD could not rule out the possibility of different binary and ternary phases that could be excluded by using Raman spectra. Thus, Raman spectroscopy analysis (inset-Fig. 1(A)) was performed to distinguish the presence of secondary phases. It shows a single peak at 332 cm^{-1} with a small hump at 287 cm^{-1} which have been attributed to kesterite Cu_2ZnSnS_4. This is due to the A1 vibrational mode of the group VI atom (S) in the lattice, where the rest of atoms remain fixed (Gürel et al., 2011). Absence of other phases, such as ZnS, $Cu_{2-x}S$, Cu_2SnS_3 and Cu_3SnS_4 indicated the pure phase of CZTS (Cheng et al., 2011).

The formation of spherical shaped nanoparticles could clearly be seen from TEM micrographs (inset(B)-Fig. 1). The size of CZTS

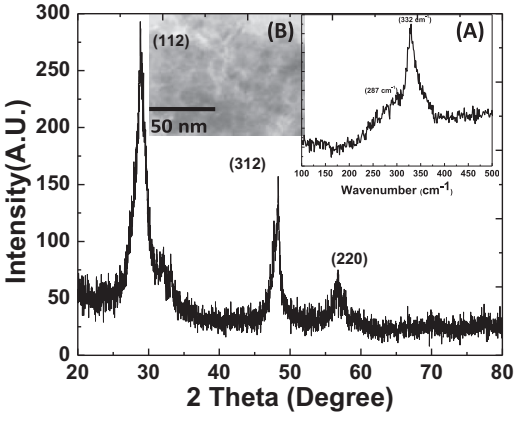

Fig. 1. XRD with inset (A)RAMAN Spectra and (B)TEM image of Butylamine-capped-CZTS nanoparticles.

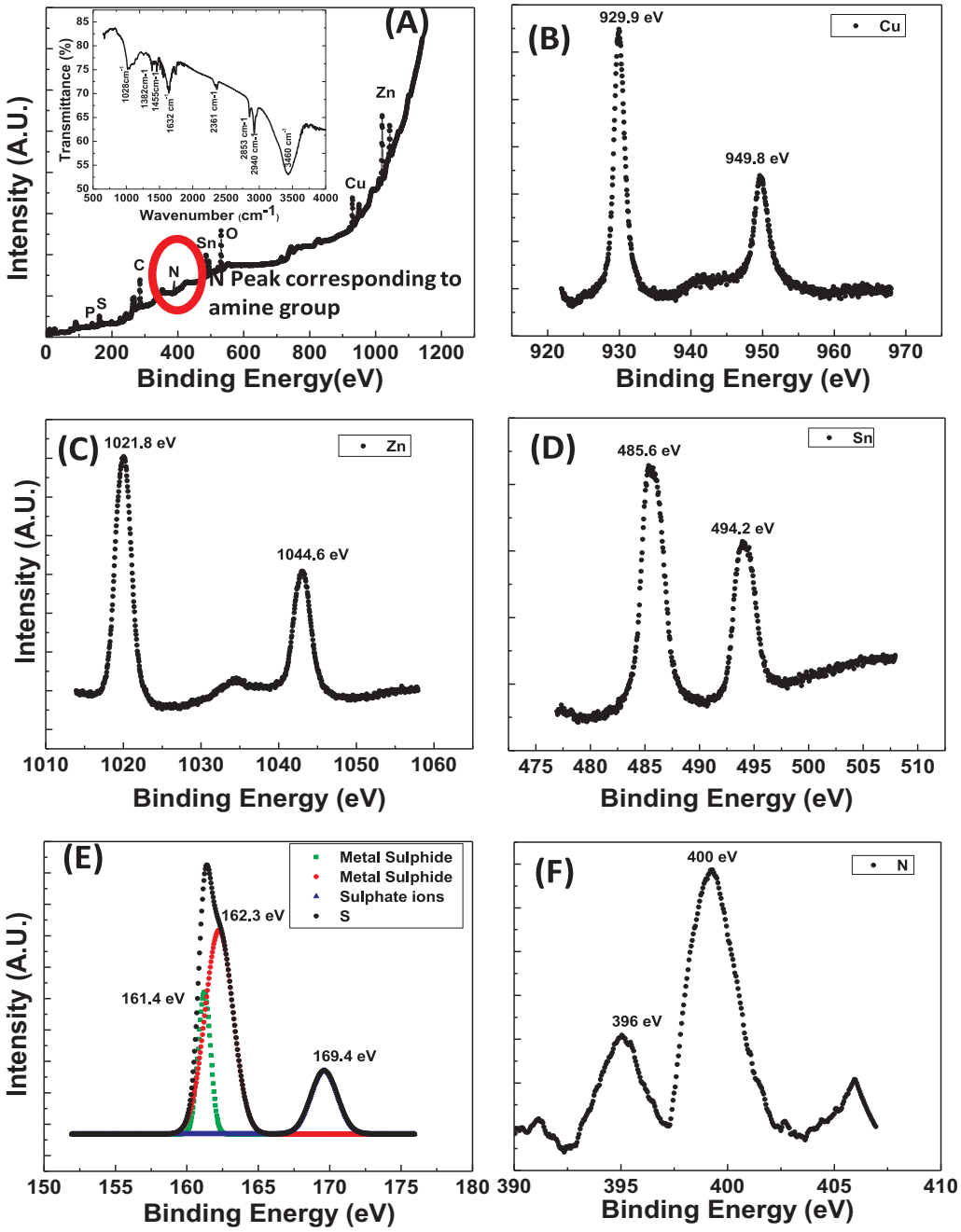

Fig. 2. Tauc's Plot (inset showing absorption-spectra) for Butylamine-capped-CZTS thin-film.

nanoparticles was found to be approximately 15 nm which matches well with the crystallite size as calculated using Debye Scherer formula, indicating the larger grain size and thus decreased grain boundaries which led to reduced recombination and trapping of charge particles (Tao et al., 2016).

HR-TEM image (Fig. SI-3(A)) shows the d-value of 0.311 nm corresponding to (112) plane, thus confirming the formation of kesterite phased spherical CZTS nanoparticles (Yin et al., 2013). Fig. SI-3(B) shows the SAED pattern for CZTS films which further confirms the highly crystalline nature of nanoparticles. The SEM images (Fig. SI-4) confirms the spherical morphology and monodispersed particles size distribution of CZTS-nanoparticles with no aggregate formation.

The chemical composition and oxidation state of CZTS nanoparticles were examined using the XPS spectra as shown in Fig. 2. Survey spectra corresponding to CZTS films shows the peak corresponding to C 1 s visible at about 284.6 eV, with various other peaks corresponding to constituting elements Cu, Zn, Sn, S, and N respectively. The corresponding high-resolution core level spectra for constituting element are also shown in Fig. 2(B-E). All the data were corrected using carbon C(1 s) as an internal energy reference. Fig. 2(B) represents the core level spectrum that exhibits peaks at 930 eV and 949.8 eV representing the Cu $2p^{3/2}$ and Cu $2p^{1/2}$ having splitting energy of $\Delta = 19.8$ eV which the + 1 Oxidation state of copper, thus confirming the formation of Cu(I) state required in the formation of CZTS nanoparticles. The peak at 930 eV is attributed to Cu-S binding in CZTS compound. Fig. 2(C) shows Zn 2p core-level spectrum exhibiting two peaks at the binding energy of 1021.8 and 1044.6 eV corresponding to Zn $2p^{3/2}$ and $2p^{1/2}$ states having a separation of 22.8 eV which is coherent with the standard splitting of 23 eV suggesting the formation of zinc in + 2 oxidation state of CZTS nanoparticles. Fig. 2(D) represents the core level spectrum corresponding to Sn which exhibits Sn $3d^{5/2}$ and Sn $3d^{3/2}$ peaks at 485.6 and 494.2 eV with a separation of ~8.6 eV, and therefore

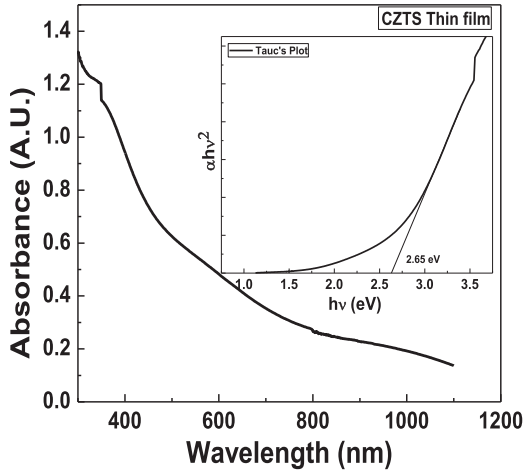

Fig. 3. (A)Survey-spectra and Core-level spectra corresponding to (B)copper (Cu), (C)Zinc(Zn), (D)Tin(Sn) and (E)Sulfur(S) and (F)Nitrogen(N) of butylamine-capped CZTS with inset showing FTIR-spectra.

confirms the formation of Sn(IV) state with well separated spin-orbit coupling in CZTS sample. Fig. 2(E) shows core level spectrum exhibiting S $2p^{3/2}$ and S $2p^{1/2}$ peaks with binding energies at 161.4 and 162.3 eV (deconvoluted Gaussian components) and a peak splitting of ~0.9 eV, which are consistent with the 160–164 eV range expected for S in sulfide phases as required information of CZTS nanoparticles. It shows that S 2p peak has closely spaced spin-orbit component. The peak at 161.4 eV shows the chalcopyrite bonding state. However, one peak is also observed at ~169 eV which shows the presence of sulfate ions at the film surface (Hurtado et al., 2014).

In survey spectra (Fig. 2(A)) we find two peaks at ~ 286 and ~399 eV which shows C-N-H binding and C-NH_2 binding respectively which is further reflected in core level spectra (Fig. 3(F)) of N1s showing two peaks at ~396 eV and ~400 eV corresponding to the metal nitride bonding and C-NH_2 bonding. Presence of metal nitride bonding confirm the capping of CZTS nanoparticles with an amine group on its surface whereas, C-NH_2 represents some unbounded butylamine in the sample (Kerber et al., 1996). The presence of amine group on the surface of CZTS nanoparticles provides the biocompatible environment for the enzyme to immobilize on the nanoparticle surface. The broad band in FTIR spectrum (inset-Fig. 2(A)) at 3450 cm^{-1} corresponds to N–H stretching vibration from the amine group present in butylamine and band at 1632 cm^{-1} represents the N-H rocking vibrations of the organic amines also confirms the presence of capping ligand butylamine. However, peaks at 1028 cm^{-1} and 1382 cm^{-1} respectively represent C-N stretching in butylamine (Mudunkotuwa et al., 2014; Tian et al., 2012).

The atomic % of constituent elements (SI-Table 1) shows the high content of Zn results into a wide bandgap of CZTS as depicted in Tauc's Plot as a requirement for good sensing material (Jain and Sharma, 2017).

3.2. Tauc's Plot (UV-Absorption curve)

The UV-absorption curve for butylamine-capped-CZTS thin-films shows broad absorption in the visible range of spectra (Fig. 3). The corresponding Tauc's plot ($\alpha h\nu^2$ Vs. $h\nu$) for CZTS nanoparticles shows the band gap value of 2.65 eV by extrapolating the linear portion of the curve to $h\nu$-axis (inset-Fig. 3). The large band gap determined from Tauc's plot is attributed to the higher incorporation of Zn as will be depicted by XPS analysis (Park et al., 2013). Due to wide band gap and presence of amine group, these nanoparticles can be used in biosensing applications.

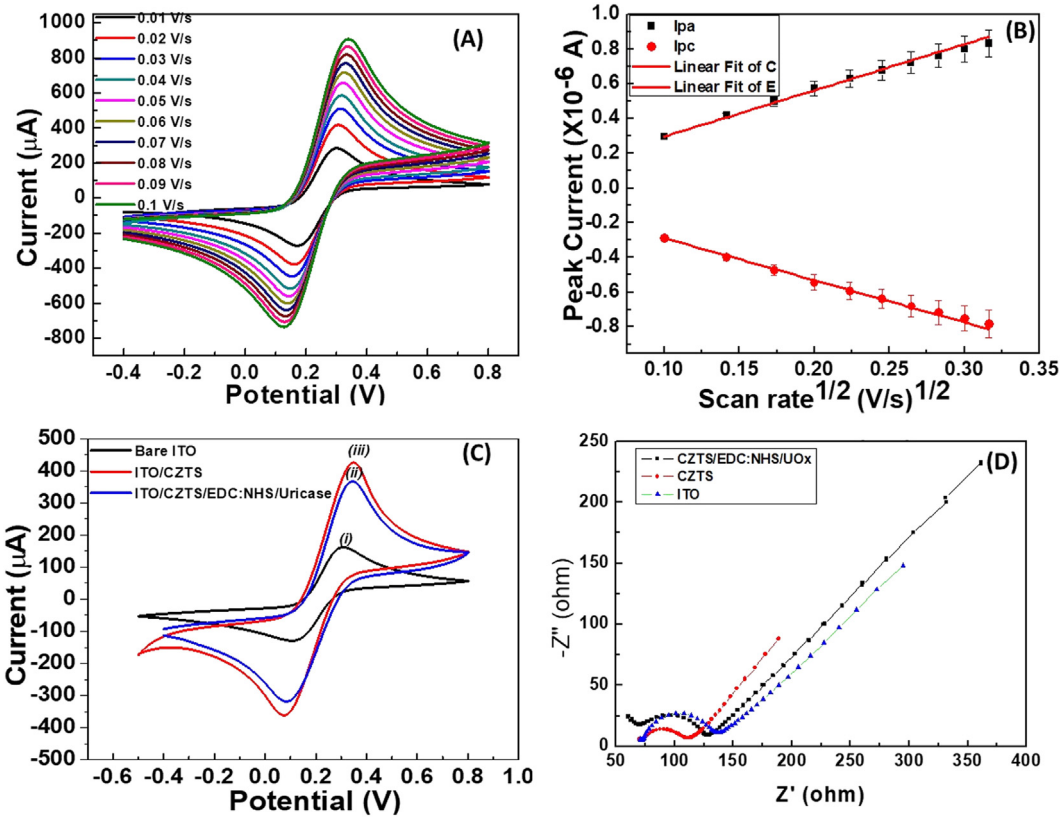

Fig. 4. (A)Scan-rate study at different scan rate (0.01–0.10 V/s), (B) Plot between peak-current and square-root of scan-rate for CZTS/ITO electrode. The electron-transfer capabilities of electrodes at each modification step using (C)CV at the scan-rate of 50 mV/s and (D)EIS technique respectively.

3.3. Electrochemical studies of bioelectrode

The electron transfer behavior of ferro-ferri redox couple at CZTS/ITO electrodes were investigated by performing cyclic voltammetry experiments in Zobell at different scan rates ranging from 10 to 100 mV/s in 3 mM Zobell (Fig. 4(A)). It shows a subsequent rise in anodic (I_{pa}) and cathodic (I_{pc}) peak currents with increasing scan rate for CZTS/ITO electrode. The ratio of forward-to-reverse peak currents (I_{pa}/I_{pc}) is calculated to be 1.0818 representing the quasi-reversible phenomenon occurring at CZTS/ITO electrode. Also, the increase in peak separation potential (ΔE) values due to shifting of oxidation peaks towards higher potential and reduction peaks towards lower potential with increasing scan-rate, further confirms the quasi-reversible process taking place at the electrode surface. The plot shown in Fig. 4(B) describes the relationship of redox peak currents with square root of scan rate values. The graph shows the linear variation of I_{pa} and I_{pc} with respect to square root of scan rates having regression coefficient (R^2) values of 0.9966 and 0.9960 respectively, suggesting the electrochemical process to be a diffusion assisted electron-transfer process (Arora et al., 2011; Jindal et al., 2013).

Cyclic voltammetry (CV) is employed to characterize and study the electrochemical performances of bare-ITO electrode at different stages of surface modification for fabrication of uric acid biosensor. Fig. 4(C) shows the CV obtained at (i)bare-ITO (ii)CZTS/ITO and (iii)UOx/EDC:NHS/CZTS/ITO at a scan-rate of 50 mV/s in 3 mM Zobell's solution. It was observed that the current corresponding to the oxidation at the CZTS deposited thin film-based electrode (425μA) is higher as compared to that of the ITO coated glass substrate (158μA) confirming the enhanced charge transport phenomenon on the deposited CZTS matrix. However, a decrease in oxidation current (373μA) was also observed after the immobilization of uricase enzyme onto the matrix surface through covalent attachment using EDC:NHS (UOx/EDC:NHS/CZTS/ITO) which is due to the non-conducting nature of uricase enzyme. The electron transfer capabilities of electrodes were further investigated using EIS-technique at each modification step (Fig. 4(D)). The charge transfer resistance (R_{CT} ± RSD) values were found to be 80.73 ± 1.86, 68.84 ± 1.04 and 71.78 ± 1.13 Ω for bare-ITO, CZTS/ITO and UOx/EDC:NHS/CZTS/ITO electrodes respectively. The lower R_{CT} value for CZTS/ITO compared to that of other electrodes confirms the quick charge transfer kinetics at the electrode/electrolyte interface, (Verma et al., 2017). The slight increase in R_{CT} for bioelectrode validate the results obtained from CV and advocate the aptness of the CZTS/ITO-matrix for immunosensor fabrication.

The analytical response of a biosensor is highly dependent on the activity of the enzyme which is extremely sensitive to the pH value of the electrolyte solution. Hence, the variation in the response of the bioelectrode towards 50 μM concentration of UA in different pH environments was analyzed. Fig. 5(B) shows the effect of varied pH value (range 6.0–8.5) of 3 mM Zobell on the oxidation peak current obtained at UOx/EDC:NHS/CZTS/ITO-bioelectrode. The response was found to increase initially as the pH changes from 6.0 to 7.0 and then starts reducing when pH value is increased further, i.e., up to 8.5. Thus, highest oxidation current was observed at pH 7.0 indicating maximum enzyme activity at this pH. So, the entire process for the development and analysis of device was carried out at the optimum pH of 7.0.

The electrochemical response studies of enzyme immobilized on CZTS working electrode has been investigated at an increasing concentration of uric acid (50–700 μM) by using CV in 3 mM Zobell at a scan rate of 50 mV/s, as shown in Fig. 5(A). Stable, increasing and quick current responses were observed for the entire range of uric acid concentrations (inset-Fig. 5(a)). The linear increase in current response was also confirmed by DPV technique (Fig. 5(c)). It occurs due to higher availability of electrons at the electrode surface as a consequence of increasing availability of uric acid for uricase catalyzed oxidation reaction in the presence of mediator as depicted in following reaction series (Fig. SI-5). The continuous enzymatic oxidation of UA causes reduction of uricase enzyme. The UOx is regenerated by reduction of ferricyanide-to-ferrocyanide ions increasing the concentration of latter at the electrode surface. The increased ferrocyanide ions undergo oxidation-reduction cycle showing increase in the redox-current.

$$UA + 2H_2O \xrightarrow{\text{Uox (oxidized)}} \text{Allantoin} + CO_2 + 2H^+ + \text{UOx (reduced)} \quad (1)$$

$$\text{Uox (reduced)} + 2[Fe(CN)_6]^{3-}\text{(ferri)} \leftrightarrow \text{UOx (Oxidized)} + 2[Fe(CN)_6]^{4-}\text{(ferro)} \quad (2)$$

$$2[Fe(CN)_6]^{4-}\text{(ferro)} \leftrightarrow 2[Fe(CN)_6]^{3-}\text{(ferri)} + 2e^- \quad (3)$$

The biosensor takes only 5 s time to give response signal for UA oxidation and subsequent reactions taking place at the electrode surface. Also, the enzyme based bioelectrodes are test for their reproducibility and found to be capable of giving identical response (with RSD-1.74) repeatedly for upto 30 times with the same biosensor indicating towards its good reusability even after one month of fabrication. The detection limit was found to be about 0.066 μM as calculated using the formula 3 $s_{y/x}$/sensitivity (Arora et al., 2011), where $s_{y/x}$ is standard deviation obtained from the oxidation peak currents of the blank measurements (in absence of UA) and is found to be 0.0408 (inset-Fig. 5(a)) whereas, sensitivity is 1.838 μA/(μM-cm^2).

The Michaelis–Menten constant (K_m) value of the biosensor was estimated to 0.13×10^{-4} M using Hanes Plot (Arora et al., 2011) (inset-Fig. 5(b)). The straight line with regression coefficient of $\sim > 0.98$ was observed. The lower K_m value indicates that present bioelectrode prepared by CZTS thin film has a high chemical attraction to the uric acid. It is due to boosted dispersion of uric acid through the surface of bioelectrode facilitated by the presence of suitable biocompatible environment due to butylamine-capping over CZTS-matrix and favorable conformational changes due to the presence of EDC:NHS in the immobilized uricase. As this is the first attempt of utilizing CZTS-nanoparticles for UA-detection using Amperometric-technique, we didn't find any difficulties during device measurements. A comparison of the already developed UA biosensors with the present work is shown in SI-Table 2 (He et al., 2018; Jin et al., 2016; Moraes et al., 2015; Wang et al., 2014; Westley et al., 2017; Zuo et al., 2015).

In real samples, the co-existence of other electroactive-biomolecules may hinder the UA detection process. Therefore, the specificity of the bioelectrode was investigated in the presence of 50 μM of each uric-acid (UA), ascorbic acid(AA), glucose, urea, and L-cystine respectively (Fig. 6). The control bar here, refers to the signal corresponding to the 3 mM Zobell (blank; without any electroactive-biomolecules). The signal corresponding to other interfering compounds is approximately same as that of blank Zobell showing no interaction of these biomolecules and enzyme. Also, the total CV-response of UA alongwith other interferents shows no significant difference from the response of UA alone signifying the higher selectivity of the fabricated biosensor towards UA.

4. Conclusion

In summary, a novel biosensing platform i.e. butylamine-capped-CZTS nanoparticles based thin film has been prepared for enzymatic detection of UA. The kesterite phased stable, biocompatible, non-toxic CZTS was synthesized using a low cost, non-vacuum hot injection technique. The increased amount of input precursor ratio Zn:Sn led to higher incorporation of Zn, resulting in enhanced band gap and thus good sensing capability. XRD and TEM analysis confirms the enhanced grain size and thus providing a large surface area for binding of enzyme and CZTS nanoparticles. The advantage of huge specific surface area in the present biocompatible CZTS accompanied by other significant properties like high carrier concentration, charge transfer capabilities with long diffusion lengths led to enhanced electrochemical activity. Working CZTS-electrodes were prepared using dip coating method

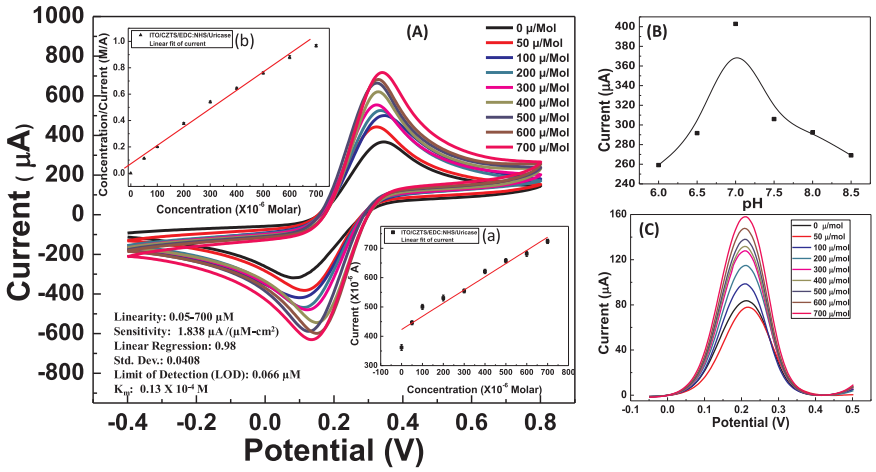

Fig. 5. (A)CV-response of UOx/EDC:NHS/CZTS/ITO (inset:(a)Current versus concentration plot and (b)Hannes Plot for Michaelis–Menten constant(K_m) respectively), (B)The effect of varied pH value of the solution on the oxidation peak and (C)DPV response of UOx/EDC:NHS/CZTS/ITO in 3 mM Zobell respectively.

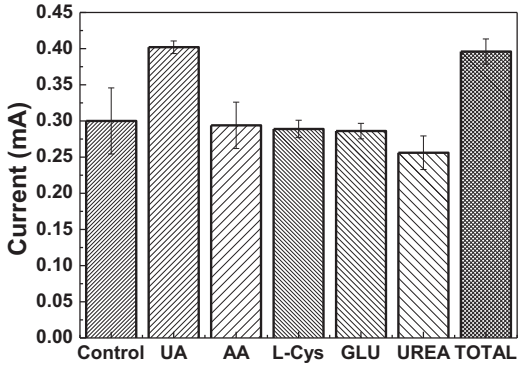

Fig. 6. Specificity test for fabricated bioelectrode with different interfering-analytes (each 50 μM) in 3 mM Zobell. The control bar specifies the signal corresponding to the blank 3 mM Zobell however, the total CV-response specifies the signal corresponding to UA plus other interfering-analyte in 3 mM Zobell.

followed by covalent immobilization of uricase enzyme onto its surface. The fabricated bioelectrodes showed high sensitivity of 1.838 μA/(μM cm^2), and fast response time of 5 s with a low detection limit of 0.066 μM as attributable to the excellent charge transfer properties of the CZTS and confirms it high potential for efficient detection of UA that can be extended for use in clinical settings. Since the present wok was the first attempt of fabricating biosensor using CZTS-chalcopyrite material, this work can further be extended or improved upon for other biosensors by amending its properties like size and shapes and also surface properties by using other biocompatible capping-ligands during synthesis.

Acknowledgment

The authors are grateful to Director, NPL for providing the facilities for completing this research work. Shefali Jain also wants to acknowledge Department of Science and Technology (DST), India for their financial assistant (PM-1019/2014) for carrying out this work.

Appendix A. Supplementary material

Supplementary data associated with this article can be found in the online version at https://doi.org/10.1016/j.bios.2018.12.008.

References

Ali, S.M.U., Ibupoto, Z.H., Kashif, M., Hashim, U., Willander, M., 2012. A potentiometric indirect uric acid sensor based on ZnO nanoflakes and immobilized uricase. Sensors 12 (3), 2787–2797.
Arora, K., Tomar, M., Gupta, V., 2011. Highly sensitive and selective uric acid biosensor based on RF sputtered NiO thin film. Biosens. Bioelectron. 30 (1), 333–336.
Chen, S., Walsh, A., Gong, X.G., Wei, S.H., 2013. Classification of lattice defects in the kesterite Cu2ZnSnS4 and Cu2ZnSnSe4 earth abundant solar cell absorbers. Adv. Mater. 25 (11), 1522–1539.
Chen, W., Cai, S., Ren, Q.-Q., Wen, W., Zhao, Y.-D., 2012. Recent advances in electrochemical sensing for hydrogen peroxide: a review. Analyst 137 (1), 49–58.
Cheng, A.-J., Manno, M., Khare, A., Leighton, C., Campbell, S., Aydil, E., 2011. Imaging and phase identification of Cu2ZnSnS4 thin films using confocal Raman spectroscopy. J. Vac. Sci. Technol. A Vac. Surf. Films 29 (5), 051203.
Chung, C., Rhee, D., Yoo, D., Choi, M., Heo, S.C., Kim, D., Choi, C., 2013. Properties of kesterite Cu2ZnSnS4 (CZTS) thin films prepared by sol-gel method using two types of solution. J. Ceram. Process Res. 14, 255–259.
Erden, Pn.E., K l ç, E., 2013. A review of enzymatic uric acid biosensors based on amperometric detection. Talanta 107, 312–323.
Goux, A., Pauporté, T., Lincot, D., 2006. Oxygen reduction reaction on electrodeposited zinc oxide electrodes in KCl solution at 70C. Electrochim. Acta 51 (15), 3168–3172.
Goyal, R.N., Gupta, V.K., Sangal, A., Bachheti, N., 2005. Voltammetric determination of uric acid at a fullerene-C60-modified glassy carbon electrode. Electroanalysis 17 (24), 2217–2223.
Gurav, K., Shin, S., Patil, U., Deshmukh, P., Suryawanshi, M., Agawane, G., Pawar, S., Patil, P., Lee, J., Lokhande, C., 2014. Cu 2 ZnSnS 4 (CZTS)-based room temperature liquefied petroleum gas (LPG) sensor. Sens. Actuators B Chem. 190, 408–413.
Gürel, T., Sevik, C., Ça n, T., 2011. Characterization of vibrational and mechanical properties of quaternary compounds Cu2ZnSnS4 and Cu2 ZnSnSe4 in kesterite and stannite structures. Phys. Rev. B 84 (20), 205201.
He, Y., Qi, F., Niu, X., Zhang, W., Zhang, X., Pan, J., 2018. Uricase-free on-demand colorimetric biosensing of uric acid enabled by integrated CoP nanosheet arrays as a monolithic peroxidase mimic. Anal. Chim. Acta 1021, 113–120.
Hurtado, M., Cruz, S., Becerra, R., Calderón, C., Bartolo-Pérez, P., Gordillo, G., 2014. XPS analysis and structural characterization of CZTS thin films prepared using solution and vacuum based deposition techniques. In: Proceedings of the 40th Photovoltaic Specialist Conference (PVSC), IEEE, pp. pp. 0368–0372.
Ibraheam, A., Al-Douri, Y., Gopinath, S., Hashim, U., 2016. A novel quinternary alloy (Cu2Zn1- xCdxSnS4) nanostructured sensor for biomedical diagnosis. Mater. Res. Express 3 (8), 085022.
Jain, S., Chawla, P., Sharma, S.N., Singh, D., Vijayan, N., 2018a. Efficient colloidal route to pure phase kesterite Cu2ZnSnS4 (CZTS) nanocrystals with controlled shape and structure. Superlattices Microstruct. 119, 59–71.
Jain, S., Sharma, S.N., 2017. Compositional Optimization of Photovoltaic Grade Cu2ZnSnS4 (CZTS) Films Synthesized by Colloidal Route. In: Jain, V., Rattan, S., Verma, A. (Eds.), Recent Trends in Materials and Devices. Springer Proceedings in Physics. 178 Springer, Cham.
Jain, S., Singh, D., Vijayan, N., Sharma, S.N., 2018b. Time-controlled synthesis mechanism analysis of kesterite-phased Cu 2 ZnSnS 4 nanorods via colloidal route. Appl. Nanosci. 1–12.
Jin, D., Seo, M.-H., Huy, B.T., Pham, Q.-T., Conte, M.L., Thangadurai, D., Lee, Y.-I., 2016. Quantitative determination of uric acid using CdTe nanoparticles as fluorescence probes. Biosens. Bioelectron. 77, 359–365.
Jindal, K., Tomar, M., Gupta, V., 2013. Nitrogen-doped zinc oxide thin films biosensor for determination of uric acid. Analyst 138 (15), 4353–4362.
Kerber, S., Bruckner, J., Wozniak, K., Seal, S., Hardcastle, S., Barr, T., 1996. The nature of hydrogen in x-ray photoelectron spectroscopy: general patterns from hydroxides to hydrogen bonding. J. Vac. Sci. Technol. A Vac., Surf. Films 14 (3), 1314–1320.

Kumar, R.S., Maddirevula, S., Easwaran, M., Dananjaya, S., Kim, M.-D., 2015. Antibacterial activity of novel Cu2 ZnSnS4 nanoparticles against pathogenic strains. RSC Adv. 5 (129), 106400–106405.
Lee, Y.S., Gershon, T., Gunawan, O., Todorov, T.K., Gokmen, T., Virgus, Y., Guha, S., 2015. Cu2ZnSnSe4 thin-film solar cells by thermal co-evaporation with 11.6% efficiency and improved minority carrier diffusion length. Adv. Energy Mater. 5 (7).
Moraes, F.C., Rossi, B., Donatoni, M.C., de Oliveira, K.T., Pereira, E.C., 2015. Sensitive determination of 17β-estradiol in river water using a graphene based electrochemical sensor. Anal. Chim. Acta 881, 37–43.
Mudunkotuwa, I.A., Al Minshid, A., Grassian, V.H., 2014. ATR-FTIR spectroscopy as a tool to probe surface adsorption on nanoparticles at the liquid–solid interface in environmentally and biologically relevant media. Analyst 139 (5), 870–881.
Nery, E. Witkowska, 2016. Analysis of Glucose, Cholesterol and Uric Acid. In: Analysis of Samples of Clinical and Alimentary Interest with Paper-based Devices. Springer Theses (Recognizing Outstanding Ph.D. Research). Springer, Cham.
Park, J., Song, M., Jung, W.M., Lee, W.Y., Kim, H., Kim, Y., Hwang, C., Shim, I.-W., 2013. Syntheses of Cu2SnS3 and Cu2ZnSnS4 nanoparticles with tunable Zn/Sn ratios under multibubble sonoluminescence conditions. Dalton Trans. 42 (29), 10545–10550.
Roushani, M., Shamsipur, M., Rajabi, H.R., 2014. Highly selective detection of dopamine in the presence of ascorbic acid and uric acid using thioglycolic acid capped CdTe quantum dots modified electrode. J. Electroanal. Chem. 712, 19–24.
Shinagawa, T., Garcia-Esparza, A.T., Takanabe, K., 2015. Insight on Tafel slopes from a microkinetic analysis of aqueous electrocatalysis for energy conversion. Sci. Rep. 5.
Shinde, S., 2015. Photocatalytic degradation of RhB and TNT and photocatalytic water splitting with CZTS microparticles. J. Semicond. 36 (7), 073003.
Tao, J., Chen, L., Cao, H., Zhang, C., Liu, J., Zhang, Y., Huang, L., Jiang, J., Yang, P., Chu, J., 2016. Co-electrodeposited Cu 2 ZnSnS 4 thin-film solar cells with over 7% efficiency fabricated via fine-tuning of the Zn content in absorber layers. J. Mater. Chem. A 4 (10), 3798–3805.
Tian, Q., Xu, X., Han, L., Tang, M., Zou, R., Chen, Z., Yu, M., Yang, J., Hu, J., 2012. Hydrophilic C2ZnSnS4 nanocrystals for printing flexible, low-cost and environmentally friendly solar cells. CrystEngComm 14 (11), 3847–3850.
Verma, S., Singh, A., Shukla, A., Kaswan, J., Arora, K., Ramirez-Vick, J., Singh, P., Singh, S.P., 2017. Anti-IL8/AuNPs-rGO/ITO as an Immunosensing Platform for noninvasive electrochemical detection of oral cancer. ACS Appl. Mater. Interfaces 9 (33), 27462–27474.
Wang, B., Xiang, H., Nakayama, T., Zhou, J., Li, B., 2017. Theoretical investigation on thermoelectric properties of Cu-based chalcopyrite compounds. Phys. Rev. B 95 (3), 035201.
Wang, C., Du, J., Wang, H., Zou, Ce, Jiang, F., Yang, P., Du, Y., 2014. A facile electrochemical sensor based on reduced graphene oxide and Au nanoplates modified glassy carbon electrode for simultaneous detection of ascorbic acid, dopamine and uric acid. Sens. Actuators B Chem. 204, 302–309.
Westley, C., Xu, Y., Thilaganathan, B., Carnell, A.J., Turner, N.J., Goodacre, R., 2017. Absolute quantification of uric acid in human urine using surface enhanced Raman scattering with the standard addition method. Anal. Chem. 89 (4), 2472–2477.
Yang, X., Xu, J., Xi, L., Yao, Y., Yang, Q., Chung, C.Y., Lee, C.-S., 2012. Microwave-assisted synthesis of Cu2ZnSnS4 nanocrystals as a novel anode material for lithium ion battery. J. Nanopart. Res. 14 (6), 931.
Yin, X., Tang, C., Chen, M., Adams, S., Wang, H., Gong, H., 2013. Hierarchical porous Cu2ZnSnS4 films for high-capacity reversible lithium storage applications. J. Mater. Chem. A 1 (27), 7927–7932.
Yoo, H., Kim, J., 2010. Growth of Cu2ZnSnS4 thin films using sulfurization of stacked metallic films. Thin Solid Films 518 (22), 6567–6572.
Zhou, W.-H., Zhou, Y.-L., Feng, J., Zhang, J.-W., Wu, S.-X., Guo, X.-C., Cao, X., 2012. Solvothermal synthesis of flower-like Cu2ZnSnS4 nanostructures and their application as anode materials for lithium-ion batteries. Chem. Phys. Lett. 546, 115–119.
Zhou, Y.-L., Zhou, W.-H., Du, Y.-F., Li, M., Wu, S.-X., 2011. Sphere-like kesterite Cu2ZnSnS4 nanoparticles synthesized by a facile solvothermal method. Mater. Lett. 65 (11), 1535–1537.
Zuo, R., Zhou, S., Zuo, Y., Deng, Y., 2015. Determination of creatinine, uric and ascorbic acid in bovine milk and orange juice by hydrophilic interaction HPLC. Food Chem. 182, 242–245.